DOI: https://doi.org/10.62985/j.huit_ojs.vol26.no1E.366

A SYNCHRONIZED DATA ACQUISITION AND STATE DETECTION SYSTEM FOR A GYROSCOPE BASED ON A BISTABLE MECHANISM

Tran Hong Van*

Ho Chi Minh City University of Industry and Trade

*Email: *vanth@huit.edu.vn*

Received: 20 March 2026; Revised: 18 May 2026; Accepted: 20 May 2026

ABSTRACT

This paper presents a comprehensive experimental framework for determining the angular-rate threshold of a bistable gyroscope. To overcome the noise and drift inherent in conventional continuous measurements, the proposed LabVIEW-based system integrates a centrifugal excitation unit controlled via Modbus RTU with a high-speed infrared sensor network. This distributed architecture detects snap-through transitions and timestamps them with millisecond resolution, enabling accurate, event-driven threshold extraction without analog signal integration. System durability and repeatability were rigorously evaluated through 100 activation cycles across 20 independent measurement sessions. Experimental results demonstrate distinct, highly consistent state transitions, with the measured threshold concentrated around 246–250 rpm. This aligns well with the 260 rpm analytical prediction, and the ~5% deviation is mainly attributed to polymer thermomechanical hysteresis and micro-machining tolerances. Ultimately, this framework offers a robust, drift-resistant measurement solution for accurately characterizing event-driven inertial sensors.

Keywords: Threshold gyroscope, LabVIEW, bistable mechanism, data acquisition, snap-through.

1. INTRODUCTION

Gyroscopes are essential inertial sensors widely used in navigation, aviation control, stabilization systems, and motion-monitoring applications [1]-[4]. In addition to conventional gyroscopes that provide continuous output signals, threshold-based gyroscopes have attracted growing attention for event-driven applications, where determining whether the angular rate exceeds a prescribed critical value is more important than continuously measuring its magnitude. Such devices can be used for early fall detection for elderly users, impact-triggered safety systems, or speed-feedback mechanisms to stabilize the gait of humanoid robots [4]-[7].

A bistable mechanism is a compliant mechanism that maintains two stable equilibrium states without continuous energy input [8]-[13]. When the external excitation exceeds a critical force, the mechanism undergoes a rapid snap-through transition between the two stable states. This behavior offers several advantages for inertial sensing applications, including elimination of mechanical backlash, low power consumption, and a clear binary output [14]-[18]. By integrating a bistable mechanism into a gyroscope, a predefined angular-rate threshold can be detected through an abrupt, observable state transition [19].

In prior work, the mechanical design and kinetostatic modeling of a bistable gyroscope were proposed and analyzed [19]. However, the practical measurement challenge, particularly the synchronized detection of the snap-through event and the corresponding angular rate, remains largely unaddressed. Reliable implementation of such a threshold-based system requires a data acquisition architecture that captures discrete state transitions with minimal delay and high repeatability.

Traditional continuous measurement methods often rely on high-speed analog-to-digital converters and numerical integration algorithms. Although these approaches are suitable for continuous sensing, they are vulnerable to drift, electrical noise, and calibration errors [1], [2], [20]. These limitations are particularly significant in event-driven inertial systems, where the accuracy of the detected transition moment directly determines the quality of the threshold measurement.

To address this challenge, the present study proposes a LabVIEW-based, synchronized data-acquisition and state-detection system for a bistable gyroscope. The framework integrates a centrifugal excitation unit controlled via Modbus RTU, an infrared optical sensor network, and a distributed microcontroller-based data-acquisition system. Rather than processing drift-prone continuous analog signals, the system detects discrete snap-through events and timestamps them in real time. The main contribution of this work is a synchronization strategy that aligns the controlled angular-rate excitation with the event-capturing algorithm, enabling robust and accurate characterization of threshold-based inertial sensors.

2. SYSTEM OVERVIEW AND THEORETICAL BACKGROUND

2.1. Dynamic Model and Threshold Condition

To accurately describe the gyroscope's dynamic characteristics, a two-degree-of-freedom lumped-parameter model is employed, as illustrated in Fig. 1 [4], [19]. The system consists of a mechanically coupled driving mode along the x-axis and a sensing mode along the y-axis. Assuming the input angular rate W_z, rotating about the z-axis is constant, the general equations of motion for the system are expressed as follows:

Driving mode:

$$(m_f + m_s)\frac{d^2x}{dt^2} + c_x\frac{dx}{dt} + k_x x = F_0\, sin(\omega_{SA}t) + 2(m_f + m_s)W_z\frac{dy}{dt} + (m_f + m_s)W_z^2 x \quad (1)$$

Sensing mode:

$$m_s\frac{d^2y}{dt^2} + c_y\frac{dy}{dt} + f(y) = -2m_s W_z\frac{dx}{dt} + m_s W_z^2 y \quad (2)$$

Where m_f and m_s are the frame mass and the effective mass of the sensing mass, respectively; c_x and c_y are the damping coefficients; k_x is the linear spring stiffness, and $f(y)$ represents the nonlinear restoring force of the bistable mechanism. The Coriolis force ($F_c = -2m_s W_z\frac{dx}{dt}$), acts as the primary excitation force in the sensing direction and is responsible for triggering the snap-through transition when the angular rate exceeds the critical threshold

The Coriolis force is generated by the coupling between the drive-mode vibration and the rotational motion and can be expressed as:

$$F_c = 2m_s W\dot{x} \quad (3)$$

where $\dot{x}$ is the drive-mode velocity, and W is the input angular rate. This Coriolis excitation serves as the primary trigger for the bistable transition.

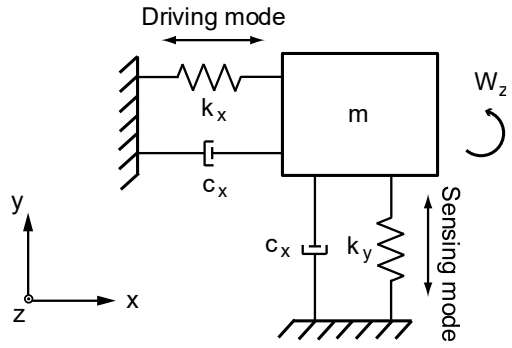

Figure 1. Two-degree-of-freedom lumped-parameter model of the threshold gyroscope.

The force-displacement characteristic curve $f(y)$ of the bistable mechanism is designed based on the Chained Beam Constraint Model (CBCM) [21]. When the Coriolis force exceeds the maximum

critical force f_{max}, the mechanism undergoes snap-through from the first stable equilibrium state S_1 to the second stable state S_2, as shown in Fig. 2 [9], [11], [12], [19].

Accordingly, the threshold condition of the gyroscope can be expressed as:

$$F_c \geq f_{max} \tag{4}$$

In the experimental setup, the gyroscope prototype is intentionally positioned at the rotational center of the centrifuge platform. As a result, the radial distance between the sensing structure and the rotation axis is approximately zero. Consequently, the centrifugal force acting on the sensing mechanism:

$$F_{cf} = m_s W^2 r \tag{5}$$

becomes negligible because r ≈ 0. Consequently, the snap-through transition is governed primarily by the Coriolis excitation rather than by centrifugal loading.

At the threshold condition, the Coriolis force reaches the maximum restoring force of the bistable mechanism.

$$F_c = f_{max} \tag{6}$$

The Coriolis force generated in the sensing direction is proportional to the centrifuge platform's rotational speed and can be expressed as:

$$F_c = \frac{4\pi m_s \dot{x}}{60} W \tag{7}$$

where m_s is the sensing mass, $\dot{x}$ is the drive-mode velocity, and W is the rotational speed in rpm.

Substituting (7) into (6), the threshold rotational speed can be obtained as:

$$W_{th} = \frac{60 f_{max}}{4\pi m_s \dot{x}} \tag{8}$$

Where W_{th} represents the minimum rotational speed required to trigger the snap-through transition in the bistable mechanism

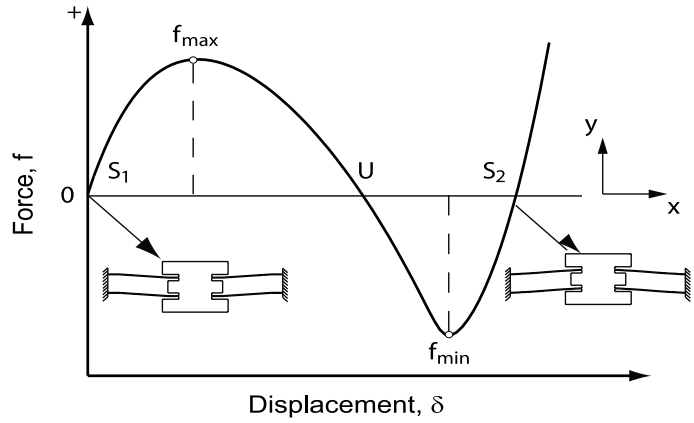

Figure 2. Force-displacement characteristics of the bistable mechanism.

2.2. Material Properties and Measurement Baseline

The prototype is fabricated from Polyoxymethylene (POM), an engineering plastic. This polymer has high mechanical strength but exhibits damping characteristics that depend on vibration amplitude and frequency [22], [23], [24]. In the ideal analytical model, the structural damping coefficient is typically assumed to be constant [25]. However, in actual high-speed operating environments, the polymer's thermomechanical hysteresis slightly affects the critical force f_{max}. The main excitation

parameters and the analytical threshold prediction are summarized in Table 1. The theoretical value of 260 rpm serves as the baseline for evaluating the accuracy of the experimental measurements.

Table 1. Excitation parameters and theoretical threshold prediction

Parameters	Symbol	Value/ Formula
Coriolis force acting on the sensing mechanism	F_{cor}	$2m_s \cdot v \cdot W$
Driving mode vibration frequency	f_d	14 Hz
Driving mode vibration amplitude	x_0	4.4 mm
Maximum critical force for snap-through	f_{max}	1.11 N
Analytical prediction of threshold angular rate	W_{th}	260 rpm

2.3. Experimental Hardware Setup

To monitor the parameters in Table 1, a hardware measurement and state detection architecture is proposed as shown in Fig. 3. This system addresses the core problem: how to controllably increase the excitation W_z to reach the threshold while simultaneously capturing the exact moment of snap-through without signal interruption or delay at high rotation speeds [17], [18], [19]. The system includes a variable-frequency drive (VFD) controlled centrifuge, magnetic actuators (Solenoids), an infrared sensor network, an Arduino MEGA 2560 microcontroller, and an ESP8266 Wi-Fi module mounted directly on the rotating disk, with an independent battery power supply.

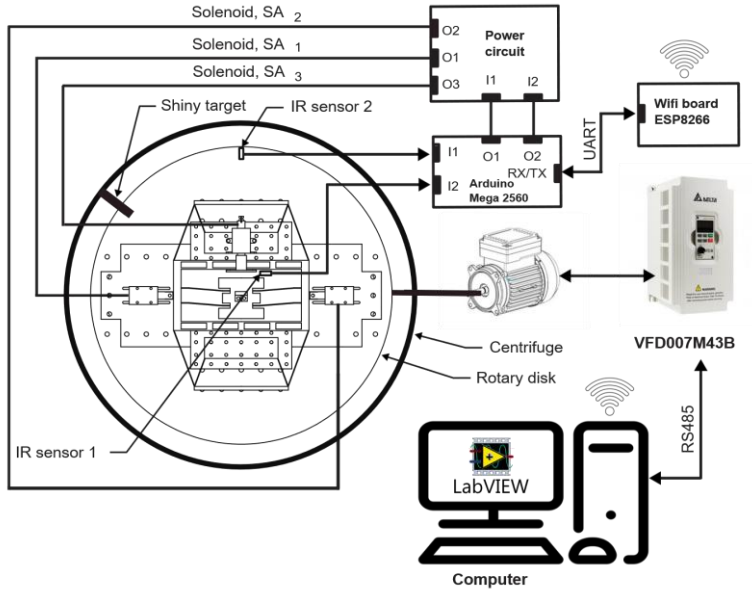

Figure 3. Schematic of the overall architecture of the measurement and data acquisition system.

3. LABVIEW-BASED SYNCHRONIZATION ALGORITHMS

3.1. Distributed Synchronized Data Acquisition and State Detection Logic

Accurate event timing is essential for threshold-based inertial sensors because the synchronization between the excitation level and the state-transition event directly determines the measured threshold [17], [18], [20].

To prevent signal delays and packet loss caused by the Wi-Fi transmission environment, the data acquisition system uses a distributed processing architecture. The Arduino MEGA 2560 manages hardware interrupts and collects high-frequency sensor data, while the ESP8266 handles TCP/IP wireless communication. The synchronization algorithm's core is the Timer1 internal timer, which generates precise interrupts every $\Delta t = 1ms$. IR Sensor 2 monitors the rotational speed (RPM). When IR Sensor 1 detects the mechanism's snap-through, the algorithm immediately stores the corresponding

time and RPM values in data arrays for transmission to LabVIEW. This logic is summarized in Algorithm 1.

***Algorithm 1**: Synchronized Data Acquisition and Time-stamping Logic*

Input: IR Sensor 1 (State transition), IR Sensor 2 (Angular rate)

Output: Data packet (RPM, t_{snap}) transmitted via ESP8266

1. Initialization

- Configure Timer1 interrupt with period $\Delta t = 1ms$.
- Initialize UART for ESP8266 (Baud rate: 115200).
- $Set\ cycle\_count \leftarrow 0, timer \leftarrow 0, RPM \leftarrow 0$

2. Interrupt Service Routine (ISR)

- Upon Timer1_Interrupt do:

$$timer \leftarrow timer + 1\ (Increment\ global\ time\ in\ ms)$$

3. Main Execution Loop

- **While Measurement_is_Running do:**
  - 3.1. Angular Rate Measurement (IR Sensor 2)
    - If IR_Sensor_2 detects LOW to HIGH transition, then:
      - $cycle\_count \leftarrow cycle\_count + 1$
    - If (timer mod 10000} = 0 then:
      - $RPM \leftarrow (cycle\_count \times 60)/10$
      - Reset *cycle_count.*
  - 3.2. State Transition Detection (IR Sensor 1)
    - If IR_Sensor_1 detects snap-through, then:
      - $t_{snap} \leftarrow timer$ (Latch millisecond timestamp).
      - Store t_{snap} in a designated array.
  - 3.3. Data Synchronization & Transmission
    - If a request is received from LabVIEW via ESP8266, then:
      - Construct packet: Packet = "<h1>3-" + RPM + "-" + t_{snap} + "#".
      - Transmit Packet via UART to ESP8266 SoftAP.
- **End While**

3.2. Modbus RTU-Based Centrifugal Control Algorithm

A Delta VFD007M43B inverter drives the centrifugal motor [26]. Speed control from LabVIEW is implemented via an RS-485 serial network using the Modbus RTU protocol. The communication parameters are configured as follows: Slave ID = 1, baud rate = 9600 bps, and data format = 8 data bits, no parity, 2 stop bits. All command frames follow the standard Modbus RTU structure with Big-Endian byte ordering and CRC-16-MODBUS error checking.

Table 2 summarizes the key registers used for motor control and monitoring. The register map consists of two functional groups. The first group includes control commands using Function Code 06H, allowing LabVIEW to send run/stop commands and set the target frequency. The second group includes monitoring registers using Function Code 03H, which are used to acquire real-time inverter status, output frequency, and motor speed. In particular, register 2105H provides the motor speed in rpm and is used to cross-reference the angular rate with the snap-through event detected by the infrared sensor.

Table 2. Key Modbus RTU registers for VFD control and monitoring

Category / Parameter	Modbus Address (Hex)	Function Code	Setting Value / Scaling	Description
I. Control Commands				
Operation Command	2000H	Write (06H)	1: Run; 2: Stop 18: Fwd; 32: Rev	Controls the motor's operational state.
Target Frequency	2001H	Write (06H)	Target Hz × 100	Sets the desired running frequency.
Fault Reset	2002H	Write (06H)	1: Reset	Clears active inverter faults.
II. Monitoring Data				
Inverter Status	2101H	Read (03H)	0: Stop; 1: Run 3: Fwd; 4: Rev	Real-time operational mode status.
Error/Fault Code	2100H	Read (03H)	0: No Error >0: Active Error Code	Current fault status.
Output Frequency	2103H	Read (03H)	Divide by 100 (Hz)	Real-time frequency applied to the motor.
Motor Speed	2105H	Read (03H)	Divide by 1 (rpm)	Estimated actual motor speed.

3.3. LabVIEW Software Design and User Interface

A LabVIEW graphical user interface was developed to implement the proposed control and data-acquisition algorithms. The software comprises two main modules: the centrifugal motor control module and the sensor/solenoid monitoring module.

The centrifugal motor control interface, shown in Fig. 4, allows the user to configure UART communication parameters, including port number, baud rate, data bits, parity, stop bits, and flow control. Once the connection is established, LabVIEW reads the inverter parameters and displays the communication status on the interface. The connection-status indicator confirms a successful connection.

The motor can be operated in either Manual Mode or Auto Mode. In Manual Mode, the user sets the target frequency and sends the command to the inverter. LabVIEW then verifies the inverter's response and updates the motor status, output frequency, output current, output voltage, and rotational speed. The control logic for Manual Mode is illustrated in Fig. 6.

In Auto Mode, the motor speed increases according to a predefined frequency array. LabVIEW sequentially sends frequency commands to the inverter at specified intervals, enabling a controlled, stepwise ramp-up. This operating mode ensures repeatable excitation conditions for threshold detection experiments. The corresponding control flowchart is shown in Fig. 7.

The second interface, shown in Fig. 8 and Fig. 9, is designed for RPM acquisition, infrared sensor monitoring, and solenoid control. After establishing a wireless connection with the Arduino–ESP8266 module, LabVIEW sends control commands to enable the solenoid, IR Sensor 1, and the RPM counter. During operation, the software continuously receives sensor status, timestamps, and RPM data. When IR Sensor 1 detects a snap-through transition, the timestamp and corresponding RPM value are displayed and recorded immediately. The data acquisition process then stops until the system is reset for the next trial.

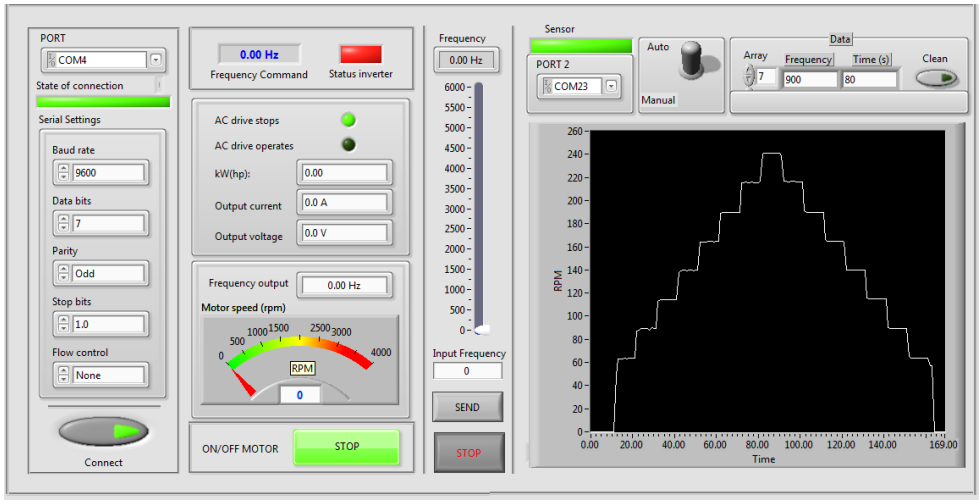

Figure 4. The centrifuge user interfaces.

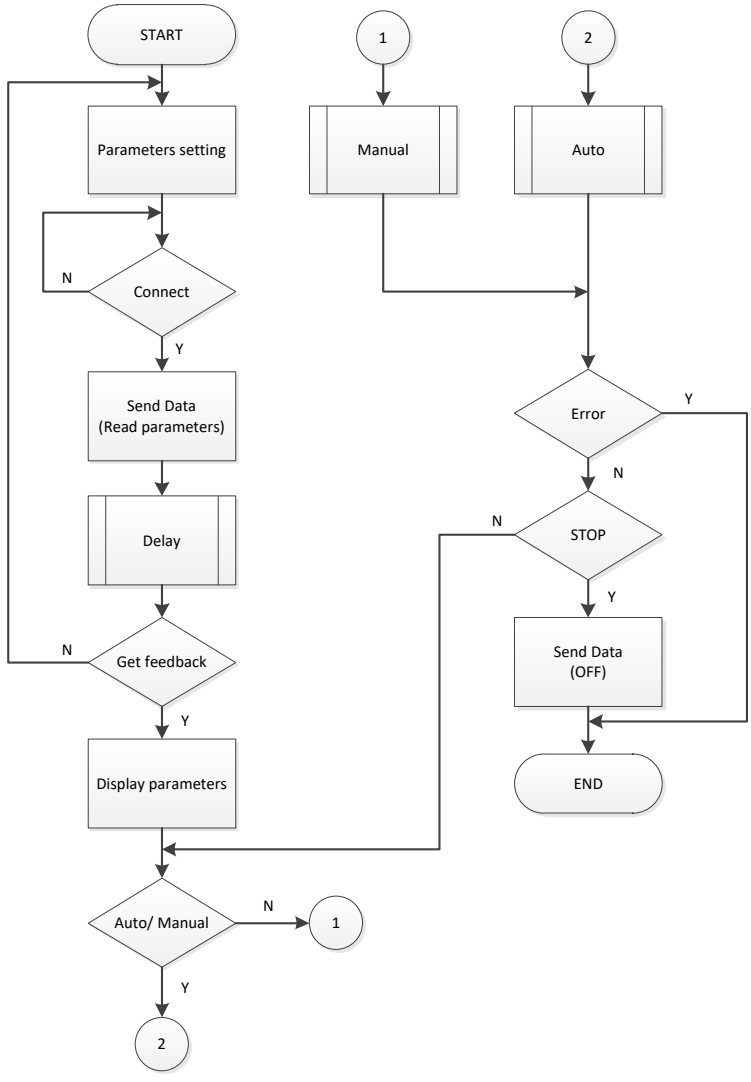

Figure 5. The flowchart of the control centrifugal

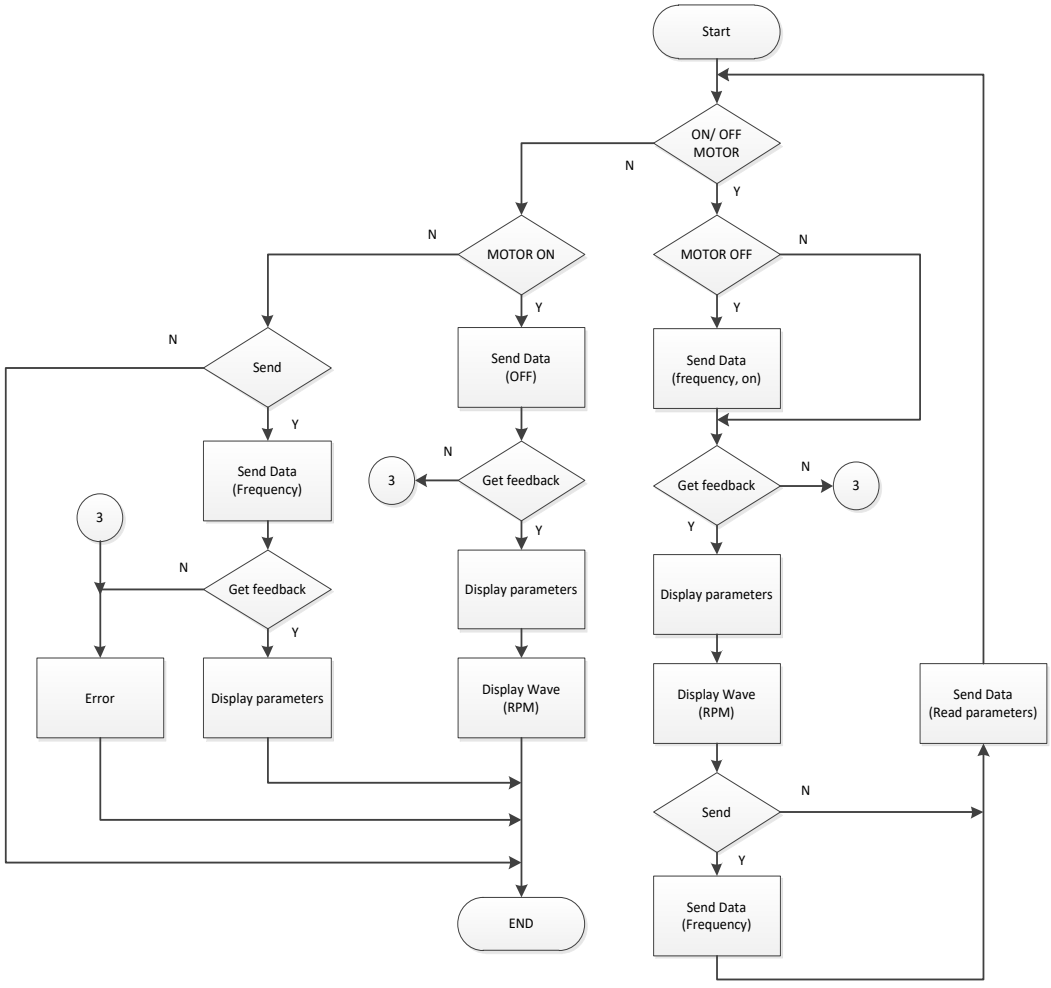

Figure 6. The flowchart of the control centrifugal in manual mode

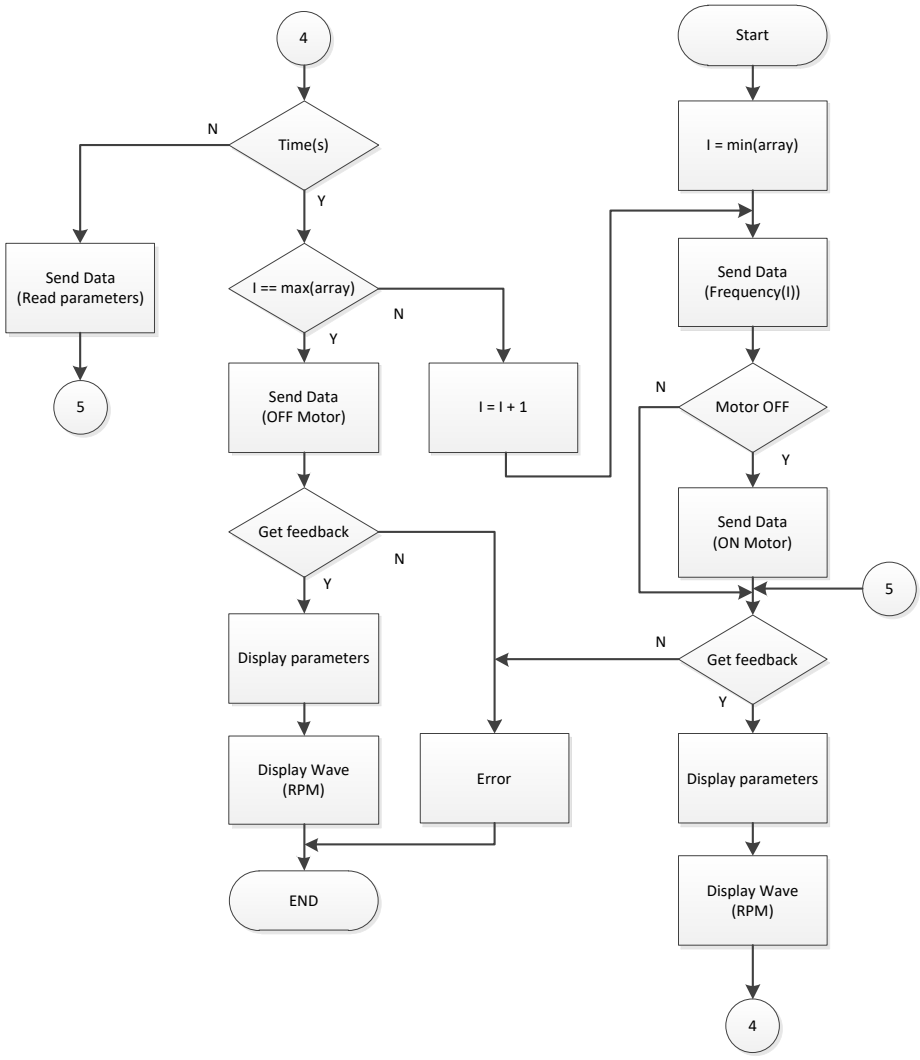

Figure 7. The flowchart of the control centrifugal in auto mode

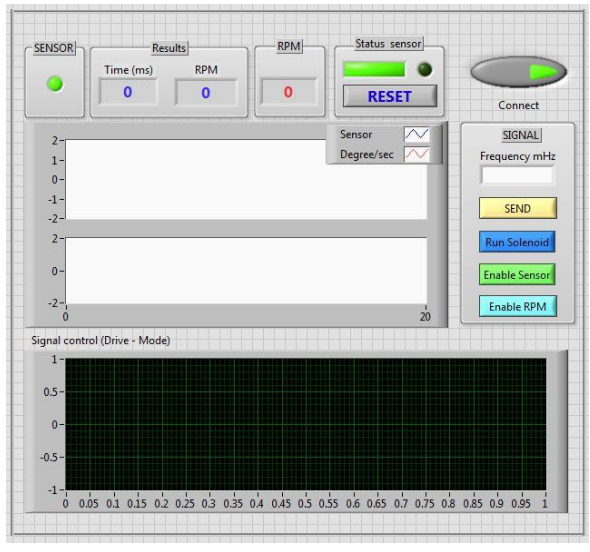

Figure 8. User interfaces for the get-data RPM, Sensor, and control solenoids

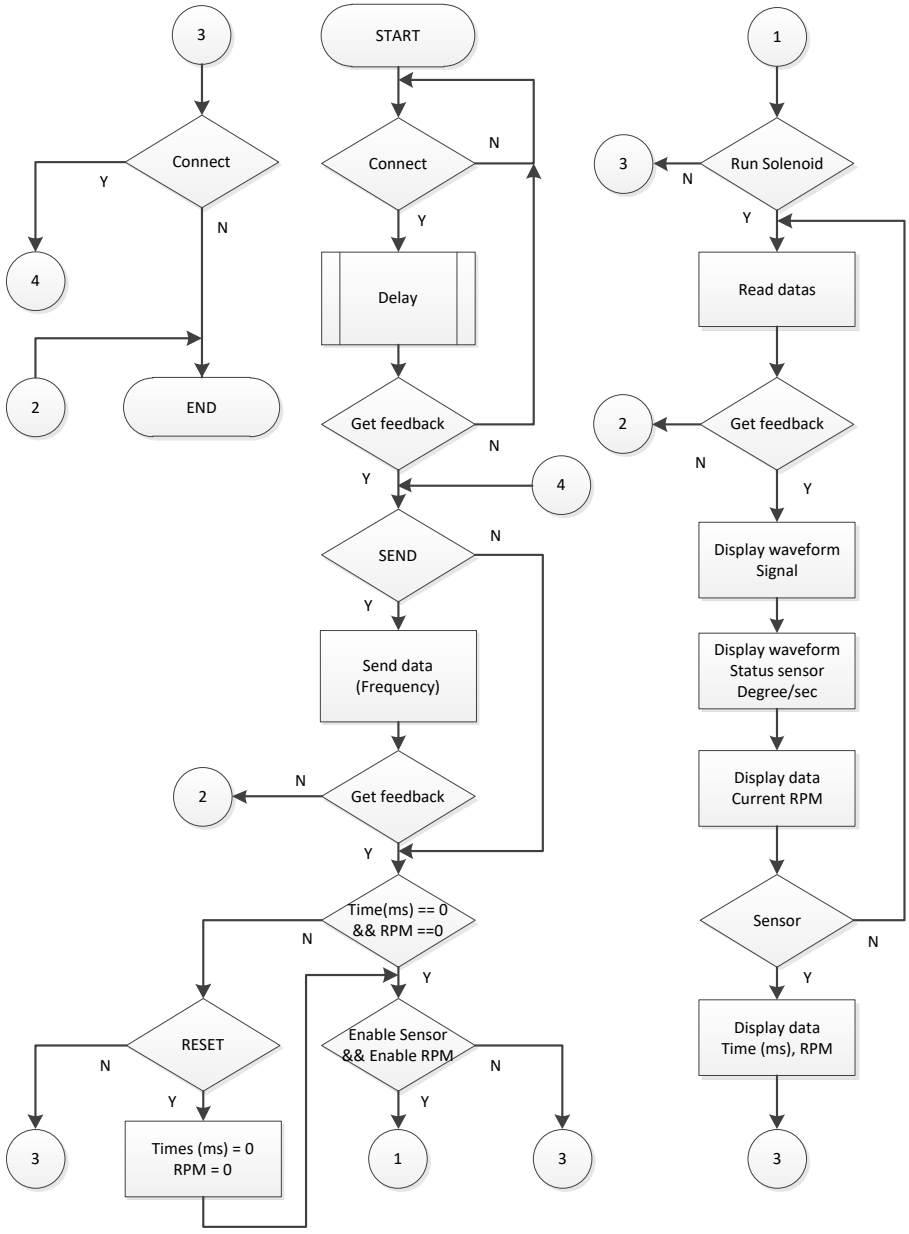

Figure 9. The flowchart of control solenoids reads data.

4. EXPERIMENTAL RESULTS AND DISCUSSION

4.1. Dynamic Response and Centrifugal Excitation Process

The system was operated in Auto Mode to ensure repeatable centrifugal excitation. Fig. 10 shows the time history of the angular-rate input. Rather than applying continuous acceleration, LabVIEW increased the angular rate in steps over a total test duration of 180 s. This stepwise ramp-up strategy provides stable excitation intervals and allows the bistable mechanism's response to be clearly observed at different angular-rate levels.

Fig. 11 shows the displacement response in the sensing direction. At low angular rates, the mechanism exhibits only local intrawell oscillation around the first stable state S_1 [18], [20], [33]. As the W_z increases, the Coriolis force increases accordingly, resulting in a larger vibration amplitude.

When the excitation becomes sufficiently high, the bistable mechanism reaches its critical condition and undergoes snap-through [12], [13], [17], [19].

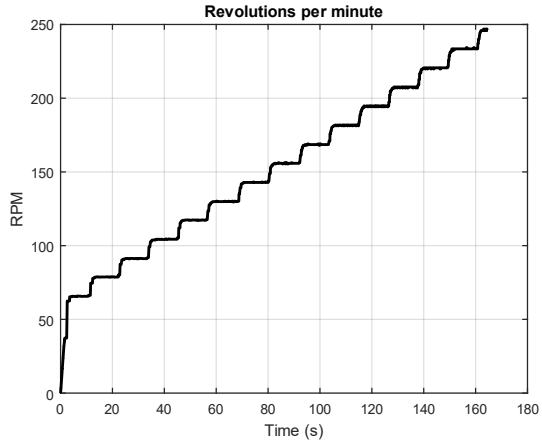

Figure 10. Time history of the angular rate input under controlled ramp-up excitation

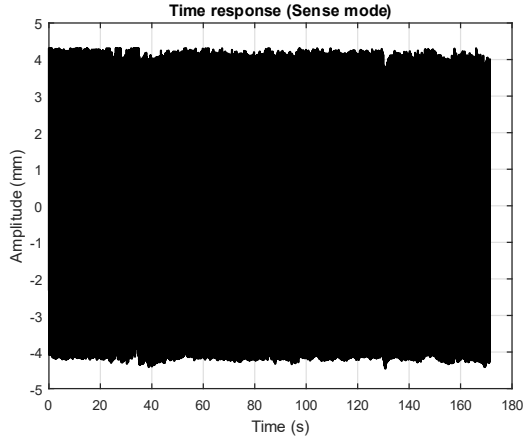

Figure 11. Time history of the displacement in the sense mode.

4.2. Snap-Through Detection and Data Synchronization

The effectiveness of the synchronized measurement system is demonstrated in Fig. 12. As shown in Fig. 12(a), the signal from IR Sensor 1 remains at zero during the initial stage of the test, indicating that the mechanism is held in the first stable state S_1.

At approximately 162 s, the enlarged view in Fig. 12(b) shows an abrupt change in the infrared sensor signal. This transition confirms that the Coriolis force has exceeded the bistable mechanism's critical force, causing the shuttle mass to snap from S_1 to S_2 [19].

Fig. 12(c) shows synchronization between the angular-rate data and the state-transition signal. As soon as the first sensor pulse is detected, the algorithm latches the corresponding timestamp and angular rate. The threshold angular rate is approximately 245–246 rpm. This result confirms that the proposed data acquisition architecture accurately captures the transition event without noticeable communication delay or signal loss.

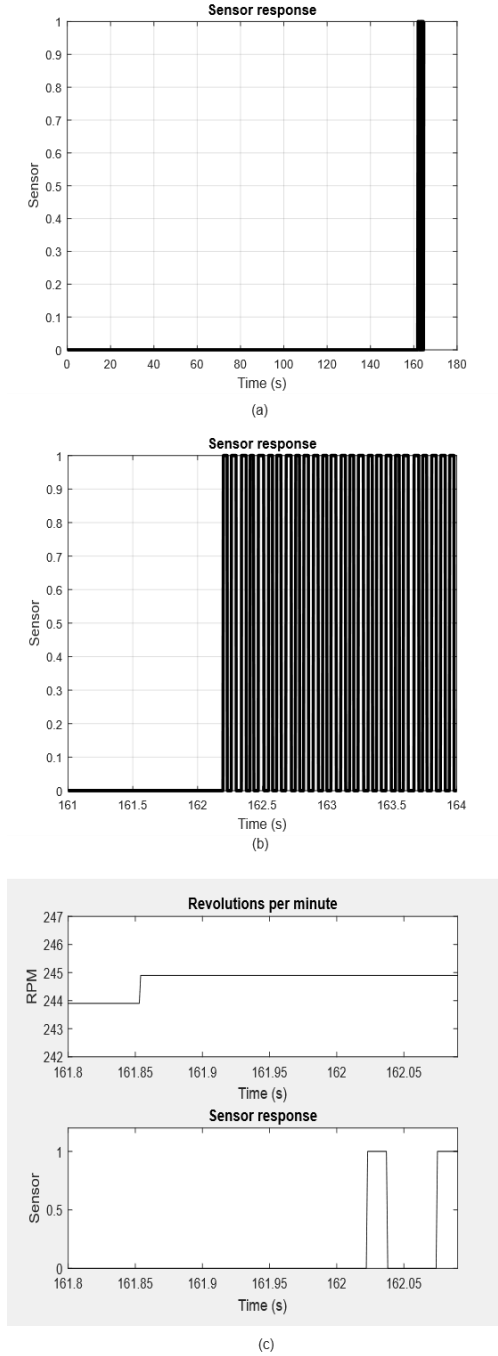

Figure 12. Sensor response and synchronized threshold detection at 246 rpm: (a) Full-scale sensor response; (b) Enlarged view of the state transition event; (c) Real-time synchronization between the angular rate and the state transition signal.

4.3. Overall Threshold Behavior

Fig. 13 summarizes the mechanism's displacement range across angular-rate levels. The result clearly demonstrates the bistable gyroscope's binary switching behavior. At angular rates below approximately 250 rpm, the mechanism remains in the first stable state, with displacement near 0 mm. Once the angular rate exceeds the threshold, the mechanism rapidly transitions to the second stable state, where the displacement reaches approximately $S_2 \approx 6.9mm$.

This behavior confirms that the bistable mechanism functions as a mechanical threshold switch, converting a continuous increase in angular rate into a discrete state transition [14]-[18].

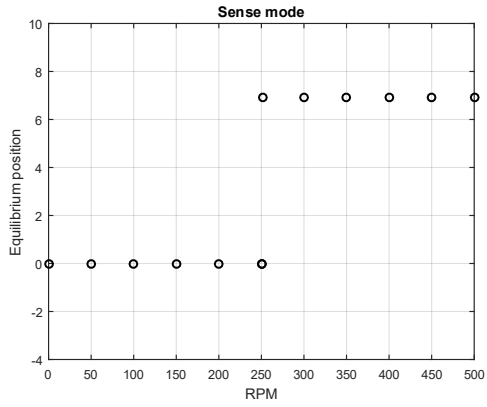

Figure 13. Binary state-transition characteristics of the mechanism under various angular rates.

4.4. Statistical Analysis and System Robustness

To evaluate mechanical durability and measurement repeatability, a statistical test series was conducted using a single hardware prototype. The experiment consisted of 20 independent measurement sessions. In each session, five consecutive threshold-sweep trials were performed in Auto Mode, yielding 100 snap-through cycles. A 15-minute rest interval was applied between sessions to reduce accumulated stress and allow partial recovery of the POM structure.

Fig. 14 shows the angular-rate threshold distribution across five consecutive trials in a representative session. The measured thresholds remain highly stable, with averages ranging from 249.55 to 254.80 rpm. The standard deviation is relatively small, ranging from approximately ±6.64 to ±8.74 rpm. The narrow distribution and stable median values indicate that the excitation trajectory and data acquisition algorithm yield high repeatability.

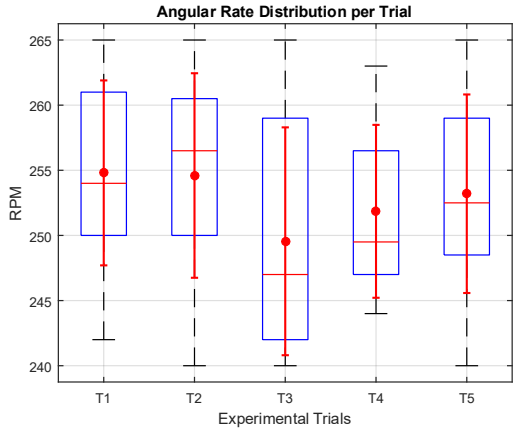

Figure 14. Boxplot showing the angular rate threshold distribution across 5 continuous trials.

Fig. 15 shows the threshold distribution across all 20 measurement sessions. The system successfully recorded all 100 snap-through events. A slight variation in the median threshold is observed across sessions. This variation is consistent with the thermomechanical behavior and damping characteristics of polymeric materials [22]-[24]. Although recovery intervals were applied, a small degree of hysteresis may remain after repeated cyclic loading, leading to minor variations in the critical force f_{max} [24].

Nevertheless, the proposed digital measurement system accurately detected every threshold-crossing event, demonstrating the algorithm's reliability.

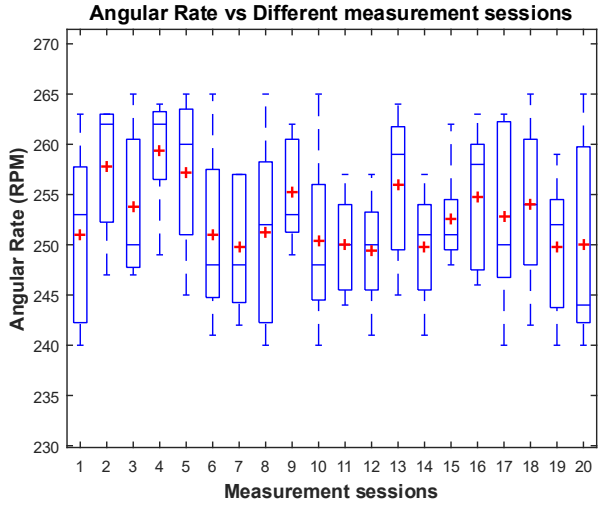

Figure 15. Boxplot illustrating the threshold variation across 20 independent measurement sessions on a single prototype.

4.5. Threshold Comparison and Error Analysis

According to the ideal analytical model, the theoretical angular rate threshold is 260 rpm. To provide a more detailed quantitative error analysis, the experimental results from 20 independent measurement samples (each with 5 trials) were statistically evaluated, as summarized in Table 3. The data show that the average measured thresholds range from 249 rpm to 259 rpm. Consequently, the relative error ranges from 1.38% to 5.45%.

Table 3. Quantitative error analysis across 20 independent measurement samples

Measurement sessions	Exp. Trial 1	Exp. Trial 2	Exp. Trial 3	Exp. Trial 4	Exp. Trial 5	Average	Error (%)
1	243	256	240	263	253	251	2.03
2	263	262	247	263	254	258	4.80
3	265	259	247	248	250	254	3.17
4	264	249	262	263	259	259	5.45
5	263	260	265	245	253	257	4.55
6	255	241	246	248	265	251	2.03
7	257	242	248	245	257	250	1.54
8	252	265	243	256	240	251	2.11
9	253	260	262	249	252	255	3.74
10	246	253	240	248	265	250	1.79
11	253	257	244	246	250	250	1.63
12	257	252	241	250	247	249	1.38
13	251	261	259	245	264	256	4.07
14	253	251	241	257	247	250	1.54
15	248	252	262	250	251	253	2.68
16	258	246	259	248	263	255	3.58
17	249	263	240	262	250	253	2.76
18	242	265	250	254	259	254	3.25
19	259	240	252	253	245	250	1.54
20	265	258	243	244	240	250	1.63

Furthermore, Table 4 presents the mean and standard deviation for the continuous experimental trials. The standard deviations range from ±6.64 to ±8.74 rpm, statistically confirming that, despite structural variation among samples, the measurement system remains highly consistent and stable.

Table 4. Mean value and standard deviation of the experimental trials

Experimental trial	Mean value	Standard deviation
1	254.80	±7.10
2	254.60	±7.85
3	249.55	±8.74
4	251.85	±6.64
5	253.20	±7.62

This maximum discrepancy of 5.45% is not random noise from the measurement system but stems from physical characteristics and manufacturing tolerances. First, the ideal model assumes a constant damping coefficient, whereas in reality, POM material exhibits complex damping behavior that depends on amplitude and frequency. Second, unavoidable micro-CNC machining tolerances introduce small geometric asymmetries, slightly reducing the actual critical force (f_{max}). Nevertheless, this quantitative error limit of ~5.45% is outstanding for macroscopic event-driven sensor prototypes. The fact that the LabVIEW distributed algorithm time-stamped the threshold moment with 100% accuracy in every trial has completely resolved the disadvantages of traditional measurement systems regarding integral signal drift.

5. CONCLUSION

A comprehensive LabVIEW-based experimental framework has been developed to determine the angular-rate threshold of a bistable gyroscope. The proposed system integrates a centrifugal excitation unit controlled via Modbus RTU, an infrared optical sensor network, and a distributed microcontroller-based data acquisition architecture to enable synchronized event detection.

Instead of relying on continuous analog signal processing, the proposed approach captures the discrete snap-through transition of the bistable mechanism and timestamps the event with millisecond resolution. Experimental results show that the measured threshold lies between 246 and 250 rpm, aligning well with the analytical prediction of 260 rpm. The approximately 5% deviation is primarily due to polymer hysteresis, damping variation, and micro-machining tolerances.

The system also demonstrated excellent repeatability and robustness over 100 activation cycles. All snap-through events were successfully detected and synchronized with the corresponding angular-rate values, confirming the reliability of the proposed measurement architecture.

Future work will focus on miniaturizing the bistable gyroscope using MEMS fabrication, integrating CMOS-based signal-processing circuits, and developing multi-threshold sensor arrays for three-axis inertial sensing. The proposed framework provides a practical foundation for event-driven inertial sensing applications in wearable medical devices, robotic stabilization systems, and threshold-based safety monitoring platforms [5]-[7], [15], [16], [18], [29].

ACKNOWLEDGMENT

The authors gratefully acknowledge the Electromechanical Energy Laboratory at National Chung Hsing University, Taiwan, and the Faculty of Electrical and Electronic Engineering at Ho Chi Minh City University of Industry and Trade for providing experimental facilities and technical support.

REFERENCES

[1] S. K. Hong and S. Park, “Minimal-Drift Heading Measurement using a MEMS Gyro for Indoor Mobile Robots,” *Sensors*, vol. 8, no. 11, pp. 7287–7299, Nov. 2008, https://doi.org/10.3390/s8117287.

[2] Z. Hu and B. J. Gallacher, “Precision mode tuning towards a low angle drift MEMS rate integrating gyroscope,” *Mechatronics*, vol. 56, pp. 306–317, Dec. 2018, https://doi.org/10.1016/j.mechatronics.2017.04.007.

[3] Y. Jeon, H. Kwon, H. C. Kim, and S. W. Kim, “Design and Development of a 3-axis Micro Gyroscope with Vibratory Ring Springs,” *Procedia Eng.*, vol. 87, pp. 975–978, 2014, https://doi.org/10.1016/j.proeng.2014.11.321.

[4] C. Acar and A. M. Shkel, *MEMS vibratory gyroscopes: Structural approaches to improve robustness*. New York, NY, USA: Springer, 2009, https://doi.org/10.1007/978-0-387-09536-3.

[5] Q. T. Huynh, U. D. Nguyen, L. B. Irazabal, N. Ghassemian, and B. Q. Tran, “Optimization of an Accelerometer and Gyroscope-Based Fall Detection Algorithm,” *J. Sens.*, vol. 2015, pp. 1–8, 2015, https://doi.org/10.1155/2015/452078.

[6] J. Baltes, S. Mcgrath, and J. Anderson, “Active Balancing Using Gyroscopes for a Small Humanoid Robot,” in Proceedings of the 2nd International Conference on Autonomous Robots and Agents (ICARA), Palmerston North, New Zealand, Nov. 2004. pp. 470–475.

[7] G. Wu, “Distinguishing fall activities from normal activities by velocity characteristics,” *J. Biomech.*, vol. 33, no. 11, pp. 1497–1500, Nov. 2000, https://doi.org/10.1016/S0021-9290(00)00117-2.

[8] L. L. Howell, “Compliant Mechanisms,” in *21st Century Kinematics*, London: Springer London, 2013, pp. 189–216. https://doi.org/10.1007/978-1-4471-4510-3_7.

[9] N. D. K. Tran and D.-A. Wang, “Design of a crab-like bistable mechanism for nearly equal switching forces in forward and backward directions,” *Mech. Mach. Theory*, vol. 115, pp. 114–129, Sep. 2017, https://doi.org/10.1016/j.mechmachtheory.2017.05.005.

[10] Q.-D. Truong, N.-D.-K. Tran, and D.-A. Wang, “Design and characterization of a mouse trap based on a bistable mechanism,” *Sens. Actuators A Phys.*, vol. 267, pp. 360–375, Nov. 2017, https://doi.org/10.1016/j.sna.2017.10.040.

[11] D.-A. Wang, J.-H. Chen, and H.-T. Pham, “A constant-force bistable micromechanism,” *Sens. Actuators A Phys.*, vol. 189, pp. 481–487, Jan. 2013, https://doi.org/10.1016/j.sna.2012.10.042.

[12] J. Qiu, J. H. Lang, and A. H. Slocum, “A Curved-Beam Bistable Mechanism,” *Journal of Microelectromechanical Systems*, vol. 13, no. 2, pp. 137–146, Apr. 2004, https://doi.org/10.1109/JMEMS.2004.825308.

[13] M. R. Brake, M. S. Baker, N. W. Moore, D. A. Crowson, J. A. Mitchell, and J. E. Houston, “Modeling and Measurement of a Bistable Beam in a Microelectromechanical System,” *Journal of Microelectromechanical Systems*, vol. 19, no. 6, pp. 1503–1514, Dec. 2010, https://doi.org/10.1109/JMEMS.2010.2076781.

[14] H. Van Tran, T. H. Ngo, N. D. K. Tran, T. N. Dang, T.-P. Dao, and D.-A. Wang, “A threshold accelerometer based on a tristable mechanism,” *Mechatronics*, vol. 53, pp. 39–55, Aug. 2018, https://doi.org/10.1016/j.mechatronics.2018.05.013.

[15] B. Todd, M. Phillips, S. M. Schultz, A. R. Hawkins, and B. D. Jensen, “RFID threshold accelerometer,” in *2008 IEEE AUTOTESTCON*, IEEE, Sep. 2008, pp. 55–59. https://doi.org/10.1109/AUTEST.2008.4662584.

[16] J. Zhao, R. Gao, Y. Yang, Y. Huang, and P. Hu, “A Bidirectional Acceleration Switch Incorporating Magnetic-Fields-Based Tristable Mechanism,” *IEEE/ASME Transactions on Mechatronics*, vol. 18, no. 1, pp. 113–120, Feb. 2013, https://doi.org/10.1109/TMECH.2011.2163725.

[17] A. Frangi, B. De Masi, F. Confalonieri, and S. Zerbini, “Threshold Shock Sensor Based on a Bistable Mechanism: Design, Modeling, and Measurements,” *Journal of Microelectromechanical Systems*, vol. 24, no. 6, pp. 2019–2026, Dec. 2015, https://doi.org/10.1109/JMEMS.2015.2462736.

[18] D. Nelson, A. Ibrahim, and S. Towfighian, “Dynamics of a threshold shock sensor: Combining bi-stability and triboelectricity,” *Sens. Actuators A Phys.*, vol. 285, pp. 666–675, Jan. 2019, https://doi.org/10.1016/j.sna.2018.11.026.

[19] H. Van Tran, T.-H. Ngo, P.-L. Chang, I.-T. Chi, N. D. K. Tran, and D.-A. Wang, "A threshold gyroscope based on a bistable mechanism," *Mechatronics*, vol. 63, p. 102280, Nov. 2019, https://doi.org/10.1016/j.mechatronics.2019.102280.

[20] Y. Chen, E. E. Aktakka, J.-K. Woo, and K. R. Oldham, "Modeling and calibration of a capacitive threshold sensor for in situ calibration of MEMS gyroscope," in *2016 IEEE International Conference on Advanced Intelligent Mechatronics (AIM)*, IEEE, Jul. 2016, pp. 999–1004. https://doi.org/10.1109/AIM.2016.7576900.

[21] F. Ma and G. Chen, "Modeling Large Planar Deflections of Flexible Beams in Compliant Mechanisms Using Chained Beam-Constraint-Model1," *J. Mech. Robot.*, vol. 8, no. 2, Apr. 2016, https://doi.org/10.1115/1.4031028.

[22] J.-L. Wojtowicki, L. Jaouen, and R. Panneton, "New approach for the measurement of damping properties of materials using the Oberst beam," *Review of Scientific Instruments*, vol. 75, no. 8, pp. 2569–2574, Aug. 2004, https://doi.org/10.1063/1.1777382.

[23] A. Pérez-Peña, A. A. García-Granada, J. Menacho, J. J. Molins, and G. Reyes, "A methodology for damping measurement of engineering materials: application to a structure under bending and torsion loading," *Journal of Vibration and Control*, vol. 22, no. 10, pp. 2471–2481, Jun. 2016, https://doi.org/10.1177/1077546314547728.

[24] J. TING and E. CRAWLEY, "Characterization of damping of materials and structures from nanostrain levels to one thousand microstrain," in *32nd Structures, Structural Dynamics, and Materials Conference*, Reston, Virigina: American Institute of Aeronautics and Astronautics, Apr. 1991. https://doi.org/10.2514/6.1991-1125.

[25] G. B. Muravskii, "On frequency independent damping," *J. Sound Vib.*, vol. 274, no. 3–5, pp. 653–668, Jul. 2004, https://doi.org/10.1016/j.jsv.2003.05.012.

[26] Inc. Delta Electronics, *VFD-M Series User Manual,* 2012.

[27] C.-T. Chuang, "Design, fabrication, and characterization of out-of-plane W-form microsprings for vertical comb electrodes capacitive sensor," *Journal of Micro/Nanolithography, MEMS, and MOEMS*, vol. 8, no. 3, p. 033021, Jul. 2009, https://doi.org/10.1117/1.3184796.

[28] G. Zhou and P. Dowd, "Tilted folded-beam suspension for extending the stable travel range of comb-drive actuators," *Journal of Micromechanics and Microengineering*, vol. 13, no. 2, pp. 178–183, Mar. 2003, https://doi.org/10.1088/0960-1317/13/2/303.

[29] A. K. Bourke and G. M. Lyons, "A threshold-based fall-detection algorithm using a bi-axial gyroscope sensor," *Med. Eng. Phys.*, vol. 30, no. 1, pp. 84–90, Jan. 2008, https://doi.org/10.1016/j.medengphy.2006.12.001.